Author/s:
Melia, HA;Dean, JW;Nguyen, TVB;Chantler, CT

Title:
Cu # #3,4 satellite spectrum with ab initio Auger-rate calculations

Date:
2023-01-13

Citation:
Melia, H. A., Dean, J. W., Nguyen, T. V. B. & Chantler, C. T. (2023). Cu # #3,4 satellite spectrum with ab initio Auger-rate calculations. Physical Review A, 107 (1), https://doi.org/10.1103/PhysRevA.107.012809.

Persistent Link:
https://hdl.handle.net/11343/333238

Cu $K\alpha_{3,4}$ satellite spectrum with *ab initio* Auger-rate calculations

H. A. Melia, J. W. Dean, T. V. B. Nguyen, and C. T. Chantler
The University of Melbourne, Parkville, Victoria 3010, Australia

(Received 11 October 2022; revised 7 December 2022; accepted 13 December 2022; published 13 January 2023)

This work investigates the capability of the multiconfiguration Dirac-Hartree-Fock (MCDHF) method in predicting the Cu $K\alpha_{3,4}$ spectrum. *Ab initio* energy eigenvalues, relative intensities, and radiative widths are calculated for the Cu $2p$ and $2s$ satellite transitions. By fitting to the most accurate experimental Cu $K\alpha_{3,4}$ spectra available, we show that our $2p$ satellite energy eigenvalues agree with experiment to within 0.35 eV and that our $2p$ shake probability agrees with the $2p$ fitted intensity to within 0.05%. Our fits suggest a $I(2s)$:$I(2p)$ satellite intensity ratio (as a percentage of the total $K\alpha$ spectrum) of 0.03(1):0.76(1) Theoretical predictions of this ratio can be examined using shake probabilities. We calculate the probability of shake-off due to the sudden creation of a $1s$ hole in Cu, yielding an *ab initio* $I(2s)$:$I(2p)$ shake probability ratio of 0.194:0.742. Using MCDHF, the rates at which hole states, created through the shake processes, depopulate via Auger transitions are determined. These results explain the apparent discrepancy between experimental satellite intensities and shake probabilities, and characterize the Cu $K\alpha_{3,4}$ spectrum with a satellite intensity ratio of 0.04(1):0.76, consistent with the experiment.

DOI: 10.1103/PhysRevA.107.012809

I. INTRODUCTION

The natural sciences are a process aiming to model physical reality with mathematical abstraction. Studies of characteristic x-ray spectra fit this paradigm well and substantial work has recently been conducted in this field, both empirically and theoretically, particularly within the $3d$ transition metals. In this work, we compare present theoretical calculations of energy eigenvalues and *ab initio* shake probabilities with previous theory and with the two highest accuracy experimental spectra. The motivation for this is twofold. First, comparison between theory and experiment is the only way to test the accuracy of a mathematical model. Second, where multiple theoretical frameworks are used, a comparison with the experimental data is the only way to determine the preferred theoretical approach. Both motivations are important for fundamental physics, relativistic quantum mechanics, and atomic physics. Further areas that benefit from this work include elemental analysis [1–3], space science [4–7], environmental science [8–11], and cultural applications [12–16].

Experimental work within recent years on $3d$ transition metals and others include Dean *et al.* on scandium [17,18]; Yilmaz on chromium, manganese, iron, and cobalt [19]; MacDonald *et al.* on zinc [20]; Koteswararao *et al.* on germanium, arsenic, selenium, and bromine [21]; and Webster *et al.* on copper and vanadium [22]. Copper has always been the most tested of the $3d$ metals and one of the key benchmarks for calibration, with recent work by Melia *et al.* [23], Mendenhall *et al.* [24], and Deutsch *et al.* [25,26]. Numerous recent studies investigated copper Kα lineshapes, intensity ratios, satellite spectra, Auger transitions, vacancy or spectator transitions, and evolution [27–37]. Specifically, the copper $K\alpha_{3,4}$ satellite spectrum has been a long-standing active area of research [38–40], located roughly 33-eV higher than the $K\alpha_1$ peak. Recent theoretical work predicting characteristic lineshapes include Dean *et al.* on scandium [41]; Nguyen *et al.* on copper [36,37]; Martins *et al.* on the widths of Zn [42]; and Ito *et al.* on Se, Y, and Zr [43]. The multiconfiguration Dirac-Hartree-Fock (MCDHF) method was used to describe other complex systems such as Fe^{2+} ions [44].

In comparing these theoretical and empirical experimental results, optical physics is able to test state-of-the-art relativistic quantum mechanics and atomic physics. This is essential if we are to extend these methods of calculations to other, more challenging, systems. High-accuracy calculations enable us to characterize spectra where the experimental data are absent. This is particularly important as industry strives to explore rare-earth metals.

There exist multiple methods to perform *ab initio* theoretical calculations for energy eigenvalues, transition amplitudes, linewidths, and shake probabilities. This work uses the MCDHF approach. Within the MCDHF framework itself there are several approaches. We demonstrate a few of these as separate hypotheses and the varying successes of these sheds light on key questions in modern atomic x-ray physics. The phenomena of interest in this work are anomalous asymmetries in characteristic x-ray radiation. The shake-off process is well attested to cause these asymmetries. However, there are still features unaccounted for. The Auger effect, and the related radiative Auger emission (RAE), where both an electron and photon are released upon the decay of a higher shell electron [45–47], may offer potential solutions for these anomalies. We perform calculations for the copper nonradiative Auger emission transition rates.

The copper atom with a vacancy in both the $1s$ and $2l$ shell is the origin of the high-energy $K\alpha_{3,4}$ spectrum [48]. Hence, $K\alpha_{3,4}$ results from transitions $[1s2p] \rightarrow [2p^2]$ and $[1s2s] \rightarrow [2s2p]$ (square parentheses denote hole states). A

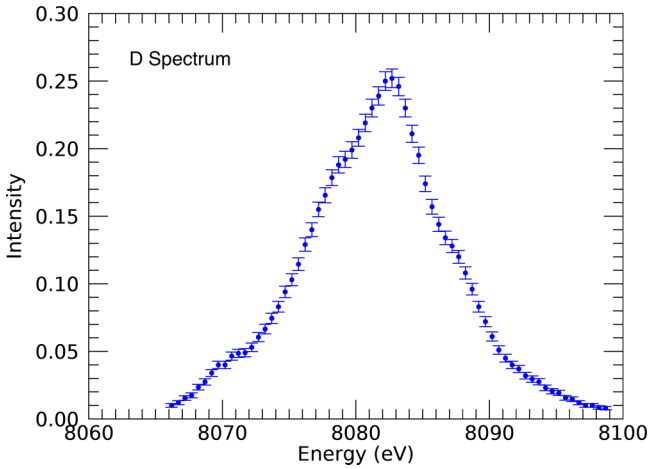

FIG. 1. The Cu $K\alpha_{3,4}$ spectrum from Deutsch *et al.* [26], which we refer to herein as the D spectrum. These data were collected to observe the evolution of the satellite spectrum with increasing incident energy.

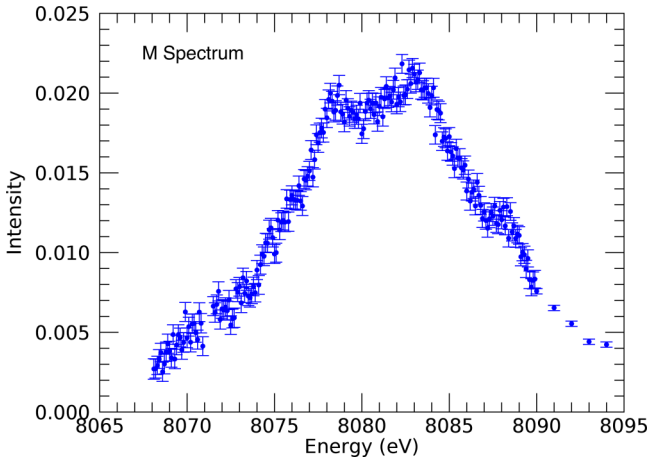

FIG. 2. The Cu $K\alpha_{3,4}$ spectrum from Mendenhall *et al.* [24], taken at the National Institute of Standards and Technology (NIST) to characterize the Cu $K\alpha$ profile. We refer to this spectrum herein as the M spectrum. This spectrum is obtained by removing the 4-Lorentzian $K\alpha_{1,2}$ characterization given by Mendenhall from the full spectrum provided as Supplemental Material [24]. Clearly the two data sets (Figs. 1, 2) are inconsistent.

major question of the literature concerns the $2p$ satellite manifold intensities and the existence of $2s$ satellites. Theoretical results suggested the $2s$ shake probability ranging from 0.1% to 1.6% [36,49]. Conversely, by fitting the experiment with theoretical predictions, other authors concluded that the $2s$ satellite does not contribute at all to Cu $K\alpha_{3,4}$ [32].

Here, we show that MCDHF for many-body systems in atomic physics allows an accurate prediction of the Cu $K\alpha_{3,4}$ spectrum, including both satellite manifolds. Including the nonradiative Auger Effect is here seen to be essential for valid physical satellite intensities. This is a major advance in providing highly accurate calculations for x-ray spectra in copper and any system with a complex open-shell structure.

II. EXPERIMENTAL DATA

The best two measurements of the $K\alpha_{3,4}$ spectral feature are those of Deutsch *et al.* [26], hereafter referred to as the D spectrum and presented in Fritsch *et al.* [32] (Fig. 1); and Mendenhall *et al.* [24], hereafter referred to as the M spectrum (Fig. 2). We digitized Fig. 3 of Fritsch *et al.* [32]. This work investigates both sets of data.

The D spectrum provides no uncertainties and only relative intensities. We define relative uncertainties such that the uncertainty at the peak is consistent with that of the M spectrum peak, yielding a similar imputed N. For the D spectrum, we then assume normally distributed statistics so that uncertainties follow $\sqrt{N}$. The normalization appears accurate to within a factor of 2. The D spectrum includes experimental (Gaussian) broadening with half width at half maximum (HWHM) = 0.8 eV [32].

While there is some agreement in the overall shape and position of spectral features, there are clear discrepancies between D and M. The most notable discrepancy is the apparent double peak in the M spectrum while the D spectrum has a clearly defined dominant single peak (Figs. 1 and 2).

The two spectra, M and D, measure the high-energy $K\alpha_{3,4}$ spectrum. For Cu, the contributing spectator vacancy transitions in this region are, in principle, the $2p^5$ satellite, $[1s2p] \rightarrow [2p^2]$, and the $2s^1$ satellite, $[1s2s] \rightarrow [2s2p]$. Each spectral peak in Figs. 1 and 2 results from the individual transitions that make up these satellite structures. The output of atomic transition calculations are typically the energy eigenvalues, the transition amplitudes, and the radiative rates. The position of the relative peaks seen in the experimental spectra are determined by the energy eigenvalues of the underlying

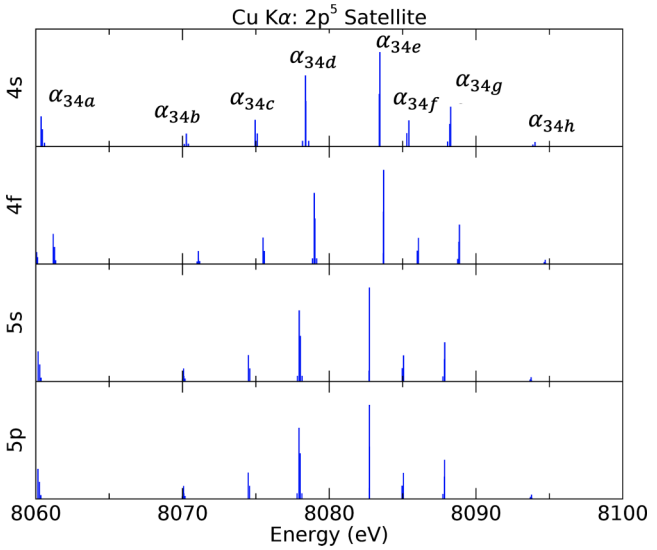

FIG. 3. The Cu $K\alpha$ $2p^5$ satellite spectral convergence. The transition amplitude gives the relative height of each transition and the energy eigenvalue gives the positions. The expansion of the active set ($4s$-reference configuration, $4f$-virtual orbitals up to the $4f$ level, $5s$ virtual orbitals up to the $5s$ level, and $5p$ virtual orbitals up to the $5p$ level) is displayed across three panels. The number of CSFs used to generate the initial- and final-state wave functions for each active set are given in Table I. As we expand the active set, we see smooth convergence of the energy eigenvalues and transition amplitudes.

TABLE I. The number of configuration state functions used to generate the initial and final state wave function for each of the $2p$ and $2s$ satellites.

		Number of CSFs	
Expansion	Active Set	Initial	Final
Cu Kα $2p$ satellite:			
$4s$	–	7	8
$4f$	$\{3s-4f\}$[a]	42 171	72 750
$5s$	$\{3s-5s\}$[a]	50 407	86 230
$5p$	$\{3s-5p\}$[a]	77 664	93 255
Cu Kα $2s$ satellite:			
$4s$	–	3	7
$4f$	$\{3s-4f\}$	9766	47 372
$5s$	$\{3s-5s\}$	11 771	56 452

[a]For the $2p$ satellite the $4s$ orbital was excluded from the active set when performing the multiconfiguration expansion.

transitions. The relative heights of these peaks are determined by the probability of each transition occurring (so they relate to the transition amplitude). The widths of the spectral features Γ_T, and therefore, the overlap between neighboring features, relate to transition rates A through $\Gamma_T = \hbar A$. The total width is determined by summing the radiative, Auger, and Coster-Kronig widths [50].

III. MULTICONFIGURATION DIRAC-HARTREE-FOCK CALCULATIONS OF THE Cu $2p$ AND Cu $2s$ SATELLITES

We recently showed that the MCDHF method is able to determine energy eigenvalues converging with the expansion of the active set to within 0.05 eV [36], and is capable of recreating experimental peak energies to within 0.1 eV [37]. To investigate Cu $K\alpha_{3,4}$, the $2p$ and $2s$ satellite spectra were predicted using GRASP2K with self-energy corrections [51–53].

In the MCDHF method the atomic state wave function is approximated using a linear combination of configuration state functions (CSF) $|\gamma PJM\rangle$:

$$\Psi = \sum_{l=0}^{L} c_l \, |\gamma_l PJM\rangle \, . \tag{1}$$

Here, P is the parity, J is the total angular momentum, and M is its projection along the z axis. γ contains all other information required to uniquely define each CSF. The mixing coefficients c_l are determined by diagonalization of the Dirac-Coulomb Hamiltonian. This occurs simultaneously with the optimization of the radial wave functions. The CSFs are built from antisymmetrized products of single electron Dirac orbitals.

A zeroth-order approximation is obtained using the ground-state electron configuration. This is referred to as the reference configuration. Because of angular momentum coupling this single configuration can utilize multiple CSFs (see Table I). Additional CSFs are obtained using the active set approach, where excited-state electron configurations are generated by allowing electron excitations into, and out of, a fixed set of orbitals. Orbitals that we allow electron excitation into are labeled *virtual orbitals* or correlation states. The systematic expansion of the active set unlocks more possible excitations, leading to more CSFs, and hence, a better approximation of the atomic-state wave function.

In this work, we expand the active set using single and double electron excitations, thus allowing for electron-electron correlations [41]. When creating the reference configuration for our initial- and final-state wave functions, each orbital is optimized during the self-consistent field method. During the multiconfiguration expansion, we use the frozen-core approximation, where, after each expansion of the active set, the already-calculated orbitals are held fixed in the self-consistent field routine and the only orbitals to be optimized are the virtual orbitals being introduced at that stage of the expansion. A more detailed description of the MCDHF method and its implementation are given in [36,41,54–56].

False convergence of energy eigenvalues is a well-known issue with any multiconfiguration approach. For all calculations presented here, the $1s-2p$ subshells are excluded from the active set during the multiconfiguration expansion. This approach has been shown to give stable, accurate results [37].

To calculate the energy eigenvalues and transition amplitudes relating to the Cu $K\alpha$ $2p^5$ satellite ($[1s2p] \rightarrow [2p^2]$), the initial $\{1s^1 2s^2 2p^5 3s^2 3p^6 3d^{10} 4s^1\}$, and final $\{1s^2 2s^2 2p^4 3s^2 3p^6 3d^{10} 4s^1\}$ state wave functions were first calculated using a single electron configuration ($4s$). The active set was then expanded by allowing virtual orbitals up to the $4f$ subshell ($3s-4f$) and lastly, to the $5s$ subshell ($3s-5s$). To ensure smooth convergence of the transition amplitudes when performing the multiconfiguration expansion, the $4s$ orbital was excluded from the active set for both the initial- and final-state wave functions. We can monitor the completeness of our wave functions by examining the results at each level of expansion (Fig. 3).

For the Cu $K\alpha$ $2s$ satellite ($[1s2s] \rightarrow [2s2p]$), the process was repeated with initial state $\{1s^1 2s^1 2p^6 3s^2 3p^6 3d^{10} 4s^1\}$ and final state $\{1s^2 2s^1 2p^5 3s^2 3p^6 3d^{10} 4s^1\}$. For this calculation, the $4s$ orbital was not excluded from the active set. Smooth convergence was shown at each level of the expansion (Fig. 4). This is the first computation for this satellite using a multiconfiguration framework expanded to the $4f$ and $5s$ levels.

For each set of calculations (the $2p^5$ and $2s^1$ satellite manifolds), the convergence of the strongest transition energy eigenvalue with the expansion of the active set is displayed in Table II. For the $2s^1$ satellite, adding the $5s$ subshell to our set of virtual orbitals (or expanding the active set from the $4f$ level to $5s$ level), changes the energy eigenvalue of the strongest transition by only 0.24 eV.

At the same level of multi-configuration expansion (virtual orbitals up to $5s$), the $2p^5$ satellite does not show this quality of convergence. Hence, for this satellite, the active set was further expanded by including virtual orbitals up to $5p$. The change in energy of the dominant transition is 0.002 eV.

Table III and Fig. 3 presents the detailed listing of energy eigenvalues E for the $2p$ satellite manifold. Notice that, unlike common and past theoretical work, there are not seven eigenvalues: There are 47 unique eigenvalues. As presented in the Supplemental Material, these are not directly represented by $^{2S+1}L_J$ since these are relativistic, even were it for the

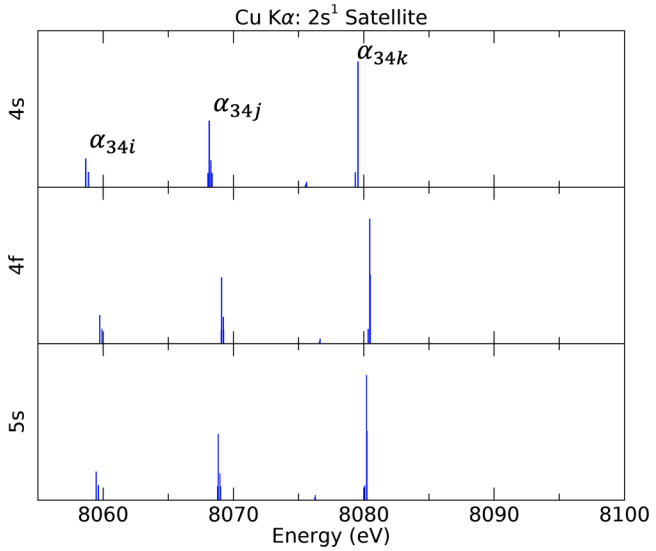

FIG. 4. Convergence of the Cu $K\alpha$ $2s^1$ satellite with the expansion of the active set.

hydrogen atom, they are good quantum numbers for $\{n\kappa\}$, J, and parity P.

Table III shows the eigenvalue convergence from $5s$ to $5p$ expansion of the active set, for all 47 transitions. The average change in the last expansion is 0.03 eV, which is strong evidence of the level of convergence with virtual orbitals up to $5p$.

Transition parameters are calculated in both the Coulomb (velocity, V) and Babushkin (length, L) gauges. A value close to 1 indicates good agreement between the two gauges. Therefore, a measure of accuracy is the gauge convergence. Table II shows the gauge convergence of the Einstein coefficient ratio A^L/A^V at each stage of our calculation for the strongest transition. Both satellites show gauge convergence to better than 1.3% for this transition. The $2s^1$ satellite requires the computation of wave functions with holes in adjacent orbitals, involving significant overlap between open-shell $n\kappa$ wave functions. This explains the lower level of agreement between the gauges for this satellite.

Tables III and IV show the gauge convergence for each of the individual transitions. For the $2p^5$ satellite, most ($\sim$95%) of the transitions show gauge convergence to better than 0.8%. It is moderately well known that forbidden or suppressed transitions have challenges with completeness for the gauge convergence ratio A^L/A^V, and this is seen in Table III for the transitions with A values (Einstein coefficients) of $10^9 s^{-1}$ and lower (contributing less than 0.002% to the final spectrum). The literature has suggested that in such cases the velocity gauge is preferred because the length gauge is sensitive to the outer part of the wave function which both converges more slowly and also overlaps with higher excitation states, though discussion continues on this topic [5,55,58].

Similarly, Table IV and Fig. 4 present the detailed listing of energy eigenvalues E for the $2s$ satellite manifold. Table IV shows the change in energy eigenvalues for all 19 $2s^1$ satellite transitions. Except for the weak transitions around 8050 eV, all transitions converge to within 0.4 eV. Similarly, the weakest transition is most susceptible to limitations in the gauge convergence.

The number of CSFs required to model each of the calculated wave functions at each stage of the multiconfiguration expansion is given in Table I.

IV. COMPARISON WITH PREVIOUS WORK

The energy eigenvalues presented in Figs. 3 and 4, and Tables III and IV, can be compared with the relativistic Dirac-Fock (RDF) energy eigenvalues [26] in their Fig. 3. Comparing the $2p^5$ satellite, there is good overall agreement between the predicted shapes of the satellite manifolds. In part, this is because the energy splitting of the $4s$ electron is small compared with the two core-hole energies. Note, our results are consistently around 1–1.3 eV smaller, both because of the more advanced and convergent computation and the full configuration.

Relativistically, states are labeled according to the total angular momentum J, parity P, and level to distinguish between states with the same J but with different spin states. Individual transitions are labeled in Tables III and IV according to these labels. The levels are defined in Tables V and VI.

When using a multiconfiguration method L and S are no longer good quantum numbers. For computational simplicity, the term symbols used when labeling the RDF transitions [26] reflect the omission of the $4s$ electron, hence modeling Cu as a Cu ion. Under this approximation, the electron configuration of Cu is $\{1s^2 2s^2 2p^6 3s^2 3d^6 3d^{10}\}$ rather than $\ldots 3d^{10} 4s^1$. By removing the $4s$ electron, Cu becomes a closed-shell system and computations become far more simple. Our calculations include all electrons and especially the $4s$ electron, and therefore, we obtain 47 individual transitions compared with 14. Note that only 7 of their 14 transitions were plotted to contribute to the spectrum. We predict seven clusters, together with additional strong clusters at low energy, around 8040 eV and 8060 eV, and weak clusters at high energy, around 8098 eV, 8103 eV, and 8111 eV. Where the authors of [26] reported a single transition, we

TABLE II. Convergence of the strongest transition for each of the $2p^5$ and $2s^1$ satellite spectra. Expanding to the $5p$ level confirms that the energy eigenvalues of the $2p^5$ satellite have converged. Gauge convergence is consistent as we expand the active set for each of the satellites. The transitions for these two satellite structures can be downloaded as text files from the Supplemental material [57].

	Single configuration ($4s$)		Expansion to $4f$		Expansion to $5s$		Expansion to $5p$	
Transition	Energy (eV)	A^L/A^V	Energy (eV)	A^L/A^V	Energy (eV)	A^L/A^V	Energy (eV)	A^L/A^V
$2p^5$ Satellite	8083.45	1.0057	8083.70 ($\pm$0.25)	1.0057	8082.74 ($\pm$0.97)	1.0055	8082.74($\pm$0.002)	1.0055
$2s^1$ Satellite	8079.55	1.0124	8080.45 ($\pm$0.90)	1.0126	8080.21 ($\pm$0.24)	1.0125		

TABLE III. Dirac (relativistic) transition quantum numbers $JP \rightarrow J'P'$, eigenvalues E, Einstein coefficient radiative rate (A), intensity (g_f), transition strength (S), the gauge ratio A^L/A^V, and the change in energy ΔE from the active set up to $5s$ to the active set up to $5p$, for all 47 Cu Kα $2p^5$ transitions for an active setup to the $5p$ orbital. Results are given in the Coulomb gauge. Cluster label relates to comparison with earlier literature. Numerals in square brackets indicate power of 10.

Level	J	P	Level′	J'	P'	Energy E (eV)	$A(s^{-1})$	g_f	S	A^L/A^V	ΔE (eV)	Cluster
1	1/2	−	1	1/2	+	8074.57	2.02[14]	1.43[−01]	7.22[−04]	1.00316	−0.0103	α_{34c}
1	1/2	−	2	1/2	+	8070.08	8.07[13]	5.71[−02]	2.89[−04]	1.00438	−0.0046	α_{34b}
1	1/2	−	3	1/2	+	8039.98	6.28[08]	4.48[−07]	2.27[−09]	0.99571	−0.1322	
2	1/2	−	1	1/2	+	8089.46	1.64[10]	1.16[−05]	5.83[−08]	1.00664	−0.0169	α_{34g}
2	1/2	−	2	1/2	+	8084.97	2.06[14]	1.45[−01]	7.35[−04]	1.00482	−0.0112	α_{34c}
2	1/2	−	3	1/2	+	8054.87	3.07[08]	2.18[−07]	1.11[−09]	0.99709	−0.1388	
3	1/2	−	1	1/2	+	8098.21	1.12[10]	7.91[−06]	3.98[−08]	0.74732	0.0132	
3	1/2	−	2	1/2	+	8093.72	2.58[13]	1.82[−02]	9.17[−05]	1.00440	0.0189	α_{34h}
3	1/2	−	3	1/2	+	8063.62	6.28[08]	4.45[−07]	2.25[−09]	1.00929	−0.1087	
1	1/2	−	1	3/2	+	8087.84	3.49[14]	2.46[−01]	1.24[−03]	1.00447	−0.0043	α_{34g}
1	1/2	−	2	3/2	+	8070.17	3.99[13]	2.82[−02]	1.43[−04]	1.00438	−0.0018	α_{34b}
1	1/2	−	3	3/2	+	8059.11	1.01[14]	7.15[−02]	3.62[−04]	1.00613	−0.0187	α_{34a}
2	1/2	−	1	3/2	+	8102.72	5.42[09]	3.81[−06]	1.92[−08]	1.00670	−0.0110	
2	1/2	−	2	3/2	+	8085.05	4.10[14]	2.89[−01]	1.46[−03]	1.00481	−0.0084	α_{34f}
2	1/2	−	3	3/2	+	8073.99	4.12[10]	2.92[−05]	1.47[−07]	1.00575	−0.0253	α_{34c}
3	1/2	−	1	3/2	+	8111.47	6.39[12]	4.47[−03]	2.25[−05]	1.00784	0.0192	
3	1/2	−	2	3/2	+	8093.80	1.22[13]	8.55[−03]	4.31[−05]	1.00428	0.0217	α_{34h}
3	1/2	−	3	3/2	+	8082.74	8.33[14]	5.88[−01]	2.97[−03]	1.00549	0.0048	α_{34e}
1	3/2	−	1	1/2	+	8064.75	8.60[10]	1.22[−04]	6.17[−07]	1.00365	−0.0190	
1	3/2	−	2	1/2	+	8060.26	1.32[14]	1.88[−01]	9.50[−04]	1.00411	−0.0133	α_{34a}
1	3/2	−	3	1/2	+	8030.15	3.68[08]	5.25[−07]	2.67[−09]	0.99726	−0.1409	
2	3/2	−	1	1/2	+	8074.48	2.08[14]	2.94[−01]	1.49[−03]	1.00317	−0.0117	α_{34c}
2	3/2	−	2	1/2	+	8069.99	1.69[13]	2.40[−02]	1.21[−04]	1.00446	−0.0060	α_{34b}
2	3/2	−	3	1/2	+	8039.89	2.92[09]	4.17[−06]	2.12[−08]	0.99611	−0.1336	
3	3/2	−	1	1/2	+	8098.18	3.13[08]	4.40[−07]	2.22[−09]	0.03140	0.0102	
3	3/2	−	2	1/2	+	8093.69	6.22[12]	8.76[−03]	4.42[−05]	1.00406	0.0159	α_{34h}
3	3/2	−	3	1/2	+	8063.59	1.02[09]	1.44[−06]	7.30[−09]	1.00629	−0.1117	
1	3/2	−	1	3/2	+	8078.01	3.61[14]	5.10[−01]	2.58[−03]	1.00390	−0.0130	α_{34d}
1	3/2	−	2	3/2	+	8060.34	2.59[13]	3.68[−02]	1.86[−04]	1.00412	−0.0105	
1	3/2	−	3	3/2	+	8049.28	5.60[13]	7.97[−02]	4.04[−04]	1.00442	−0.0274	
2	3/2	−	1	3/2	+	8087.74	3.62[13]	5.10[−02]	2.57[−04]	1.00447	−0.0057	α_{34g}
2	3/2	−	2	3/2	+	8070.07	9.96[13]	1.41[−01]	7.13[−04]	1.00440	−0.0032	α_{34b}
2	3/2	−	3	3/2	+	8059.01	9.44[12]	1.34[−02]	6.78[−05]	1.00617	−0.0201	
3	3/2	−	1	3/2	+	8111.45	6.51[11]	9.12[−04]	4.59[−06]	1.00775	0.0161	
3	3/2	−	2	3/2	+	8093.78	3.10[13]	4.36[−02]	2.20[−04]	1.00428	0.0187	α_{34h}
3	3/2	−	3	3/2	+	8082.72	8.39[13]	1.18[−01]	5.98[−04]	1.00549	0.0018	α_{34e}
1	3/2	−	1	5/2	+	8078.13	4.22[13]	5.96[−02]	3.01[−04]	1.00390	−0.0090	α_{34d}
1	3/2	−	2	5/2	+	8049.30	5.97[12]	8.49[−03]	4.30[−05]	1.00436	−0.0267	
2	3/2	−	1	5/2	+	8087.87	3.11[14]	4.38[−01]	2.21[−03]	1.00447	−0.0016	α_{34g}
2	3/2	−	2	5/2	+	8059.03	9.03[13]	1.28[−01]	6.49[−04]	1.00613	−0.0194	
3	3/2	−	1	5/2	+	8111.57	5.81[12]	8.13[−03]	4.09[−05]	1.00784	0.0202	
3	3/2	−	2	5/2	+	8082.74	7.52[14]	1.06[00]	5.36[−03]	1.00550	0.0025	α_{34e}
1	5/2	−	1	3/2	+	8077.81	2.74[13]	5.80[−02]	2.93[−04]	1.00389	−0.0204	α_{34d}
1	5/2	−	2	3/2	+	8060.14	1.57[14]	3.35[−01]	1.70[−03]	1.00410	−0.0178	α_{34a}
1	5/2	−	3	3/2	+	8049.08	4.02[12]	8.58[−03]	4.35[−05]	1.00441	−0.0347	
1	5/2	−	1	5/2	+	8077.93	3.78[14]	8.00[−01]	4.04[−03]	1.00389	−0.0163	α_{34e}
1	5/2	−	2	5/2	+	8049.10	5.72[13]	1.22[−01]	6.19[−04]	1.00440	−0.0340	

calculate a group of transitions. We note that one of their labels should be $^3P_0$ rather than $^1P_0$ [26,32]. They align the four main features of their experimental spectra as $\alpha' \equiv {}^3P_1 \rightarrow {}^3P_1$; $\alpha_3 \equiv {}^3P_2 \rightarrow {}^3P_2$; $\alpha_4 \equiv {}^1P_1 \rightarrow {}^1D_2$; $\alpha'_3 \equiv {}^3P_1 \rightarrow {}^3P_2$; with weaker plotted but not observed contributions from $^3P_1 \rightarrow {}^3P_0$; $^3P_1 \rightarrow {}^3P_0$; $^1P_0 \rightarrow {}^3P_1$ (should be $^3P_0 \rightarrow {}^3P_1$); and $^1P_1 \rightarrow {}^3P_1$ spin crossover. Their energies required a shift of about 1 eV to fit their experimental spectrum, which we note is about the improvement of our convergence and the shift of our eigenvalues. We can match each of our groups of transitions to the corresponding single transition [26].

The clusters of the transition labeled in Figs. 3 and 4 are labeled in Tables III and IV. Table VII shows explicitly

TABLE IV. Dirac (relativistic) transition quantum numbers $JP \rightarrow J'P'$, energy eigenvalues (E), radiative rate (A), intensity (g_f), transition strength (S), the gauge ratio A^L/A^V, and the change in energy ΔE from an active setup to $4f$ to an active set up to $5s$, for each of the 19 Cu Kα $2s^1$ transitions, for an active set up to the $5s$ orbital results are given in the Coulomb gauge. Numerals in square brackets indicate power of 10.

Initial State			Final State									
Level	J	P	Level′	J'	P'	Energy E (eV)	$A(s^{-1})$	g_f	S	A^L/A^V	ΔE (eV)	Cluster
1	1/2	+	1	1/2	−	8,068.96	1.96[14]	1.39[−01]	7.03[−04]	1.01260	−0.25	α_{34j}
1	1/2	+	2	1/2	−	8,059.64	1.08[14]	7.64[−02]	3.87[−04]	1.01264	−0.27	α_{34i}
1	1/2	+	3	1/2	−	8,053.14	1.68[10]	1.19[−05]	6.05[−08]	1.01305	3.03	
2	1/2	+	1	1/2	−	8,076.24	1.66[13]	1.18[−02]	5.94[−05]	1.00285	−0.37	
2	1/2	+	2	1/2	−	8,066.91	3.49[06]	2.47[−09]	1.25[−11]	1.27264	−0.39	
2	1/2	+	3	1/2	−	8,060.42	1.89[09]	1.34[−06]	6.77[−09]	1.00283	2.91	
1	1/2	+	1	3/2	−	8,080.25	5.16[14]	3.64[−01]	1.84[−03]	1.01255	−0.24	α_{34k}
1	1/2	+	2	3/2	−	8,069.01	1.01[14]	7.16[−02]	3.62[−04]	1.01264	−0.24	α_{34j}
1	1/2	+	3	3/2	−	8,053.64	3.19[06]	2.26[−09]	1.15[−11]	1.11487	3.07	
2	1/2	+	1	3/2	−	8,087.53	4.98[09]	3.51[−06]	1.77[−08]	1.01825	−0.36	
2	1/2	+	2	3/2	−	8,076.28	3.46[13]	2.45[−02]	1.24[−04]	1.00309	−0.36	
2	1/2	+	3	3/2	−	8,060.92	3.86[09]	2.74[−06]	1.39[−08]	1.00250	2.95	
1	3/2	+	1	1/2	−	8,068.79	5.04[13]	7.14[−02]	3.61[−04]	1.01261	−0.27	α_{34j}
1	3/2	+	2	1/2	−	8,059.46	1.05[14]	1.49[−01]	7.54[−04]	1.01263	−0.28	α_{34i}
1	3/2	+	3	1/2	−	8,052.97	7.40[10]	1.05[−04]	5.33[−07]	1.01054	3.02	
1	3/2	+	1	3/2	−	8,080.08	5.32[13]	7.51[−02]	3.79[−04]	1.01254	−0.26	α_{34k}
1	3/2	+	2	3/2	−	8,068.83	2.46[14]	3.48[−01]	1.76[−03]	1.01261	−0.26	α_{34j}
1	3/2	+	3	3/2	−	8,053.47	1.80[10]	2.55[−05]	1.29[−07]	1.00807	3.06	
1	3/2	+	1	5/2	−	8,080.21	4.66[14]	6.59[−01]	3.33[−03]	1.01254	−0.24	α_{34k}

the correspondence between our clusters of transitions, the ($4s$-omitted) term symbols used to label the RHF transitions calculated by Deutsch *et al.* [26] and the components of the empirical 4-Lorentzian fit labeled by Mendenhall *et al.* [24].

As well as comparing with previously calculated energy eigenvalues, we can compare with the empirical fits of $K\alpha_{3,4}$. That of [26,32] is given above and the labeling is broadly consistent with labeling since the first observation. The high-accuracy 4-Lorentzian fit of Mendenhall *et al.* [24] (their Fig. 19 and Table 4) are simply labeled $K\alpha_{31}$, $K\alpha_{32}$, $K\alpha_{33}$, and $K\alpha_{34}$. The $K\alpha_{33}$ Lorentzian models the two low-energy groups at 7070 and 7074 eV. $K\alpha_{31}$ models the group at 8074 eV. The $K\alpha_{32}$ Lorentzian models the dominant transitions at 8083 eV and the three high-energy (low amplitude) groups are modeled by $K\alpha_{34}$.

V. FITTING EXPERIMENTAL DATA WITH THEORY

To compare our MCDHF calculations to the experimental spectra of Deutsch *et al.* [26] and [24] we can use the energy eigenvalues, transition amplitudes, and radiative widths to create a simulated x-ray spectrum resulting from the Cu $2p^5$ and $2s^1$ satellite transitions. To model the nonradiative pathways an additional width is required. This width is determined using least-squares regression. To test the accuracy of our energy eigenvalues we allow an additional fitted parameter to shift the

TABLE V. Electron configurations, level, total angular momentum (J), parity (P), and dominant term symbol for the initial state wave functions and the final-state wave functions for the $2p$ satellite. As we expand the active set (i.e., move beyond the reference configuration approximation), these configurations become the leading term in the sum of CSFs that make up our wave functions. L and S are no longer well defined and the term symbols no longer represent the full atomic state wave function. States are uniquely defined by their electron configurations and angular momentum coupling. The electron configuration is given in terms of the hole states. The brackets within the electron configurations distinguish the total angular momentum of the first two holes. This defines each of the level, J, P states from Table III.

Initial					Final				
Hole configuration	Level	J	P	Term	Hole configuration	Level′	J'	P'	Term
$[1s^{-1}2p_-^{-1}]_{(0)}4s^{-1}$	1	1/2	−	$^2P_{1/2}$	$2p_-^{-2}4s^{-1}$	1	1/2	+	$^2S_{1/2}$
$[1s^{-1}2p_-^{-1}]_{(1)}4s^{-1}$	2	1/2	−	$^2P_{1/2}$	$[2p_-^{-1}2p_+^{-1}]_{(1)}4s^{-1}$	2	1/2	+	$^2P_{1/2}$
$[1s^{-1}2p_-^{-1}]_{(1)}4s^{-1}$	1	3/2	−	$^2P_{3/2}$	$[2p_-^{-1}2p_+^{-1}]_{(1)}4s^{-1}$	1	3/2	+	$^2P_{3/2}$
$[1s^{-1}2p_+^{-1}]_{(1)}4s^{-1}$	2	1/2	−	$^4P_{1/2}$	$[2p_-^{-1}2p_+^{-1}]_{(2)}4s^{-1}$	2	3/2	+	$^4P_{3/2}$
$[1s^{-1}2p_+^{-1}]_{(1)}4s^{-1}$	3	3/2	−	$^2P_{3/2}$	$[2p_-^{-1}2p_+^{-1}]_{(2)}4s^{-1}$	1	5/2	+	$^4P_{5/2}$
$[1s^{-1}2p_+^{-1}]_{(2)}4s^{-1}$	3	3/2	−	$^4P_{3/2}$	$[2p_+^{-2}]_{(0)}4s^{-1}$	3	1/2	+	$^4P_{1/2}$
$[1s^{-1}2p_+^{-1}]_{(2)}4s^{-1}$	1	5/2	−	$^4P_{5/2}$	$[2p_+^{-2}]_{(2)}4s^{-1}$	3	3/2	+	$^2D_{3/2}$
					$[2p_+^{-2}]_{(2)}4s^{-1}$	2	5/2	+	$^2D_{5/2}$

TABLE VI. Electron configurations, level, total angular momentum (J), parity (P), and dominant term symbol for the initial state wave functions and the final-state wave functions for the $2s$ satellite manifold. As we expand the active set (i.e., move beyond the reference configuration approximation), these configurations become the leading term in the sum of CSFs that make up our wave functions. L and S are no longer well defined and the term symbols no longer represent the full atomic state wave function. States are uniquely defined by their electron configurations and angular momentum coupling. The electron configuration is given in terms of the hole states. The brackets within the electron configurations distinguish the total angular momentum of the first two holes. This defines each of the level, J, P states in Table IV.

Initial					Final				
Hole configuration	Level	J	P	Term	Hole configuration	Level′	J'	P'	Term
$[1s^{-1}2s^{-1}]_{(0)}4s^{-1}$	1	1/2	+	$^2S_{1/2}$	$[2s^{-1}2p_-^{-1}]_{(0)}4s^{-1}$	1	1/2	−	$^2P_{1/2}$
$[1s^{-1}2s^{-1}]_{(1)}4s^{-1}$	2	1/2	+	$^4S_{1/2}$	$[2s^{-1}2p_-^{-1}]_{(1)}4s^{-1}$	2	1/2	−	$^2P_{1/2}$
$[1s^{-1}2s^{-1}]_{(1)}4s^{-1}$	1	3/2	+	$^4S_{3/2}$	$[2s^{-1}2p_-^{-1}]_{(1)}4s^{-1}$	1	3/2	−	$^2P_{3/2}$
					$[2s^{-1}2p_+^{-1}]_{(1)}4s^{-1}$	3	1/2	−	$^4P_{1/2}$
					$[2s^{-1}2p_+^{-1}]_{(1)}4s^{-1}$	2	3/2	−	$^2P_{3/2}$
					$[2s^{-1}2p_+^{-1}]_{(2)}4s^{-1}$	3	3/2	−	$^4P_{3/2}$
					$[2s^{-1}2p_+^{-1}]_{(2)}4s^{-1}$	1	5/2	−	$^4P_{5/2}$

energy of our simulated spectrum. This shift is then a measure of how accurately our MCDHF energies have converged to the experimentally measured spectral feature.

To create our simulated spectrum each eigenvalue is a Lorentzian with centroids given by the energy eigenvalue and intensity (integrated area) given by the transition amplitude (represented by the heights of the sticks in Figs. 3 and 4). The sum of all these N transitions gives the profile for a particular multiplet (a set of transitions within a satellite)

$$I_m(E) = A_m \sum_{n=1}^{N} L(E; \gamma_n + \gamma_m, E_n - s_m, b_n), \qquad (2)$$

where γ_n, E_n, and b_n refer to the radiative width, energy eigenvalue, and transition amplitude of the nth transition within the multiplet. These parameters are fixed by MCDHF theory. γ_m and S_m are the nonradiative width and energy shift, common to all transitions within the multiplet. Where multiple satellites contribute to the spectrum, shake probabilities give information on the relative intensities A_m. Therefore, the full model sums over M multiplets

$$I(E) = \sum_{m=1}^{M} A_m \sum_{n=1}^{N} L(E; \gamma_n + \gamma_m, E_n - s_m, b_n). \qquad (3)$$

Because the M spectrum $K\alpha_{3,4}$ feature was measured and reported along with the total Cu $K\alpha$ spectrum, the contribution of each satellite to the total Cu $K\alpha$ spectrum can be determined. To isolate the $K\alpha_{3,4}$ spectral feature the $K\alpha_{1,2}$ spectrum was modeled and then subtracted from the experimental spectrum. The fitted integrated intensity (or area) of the subtracted $K\alpha_{1,2}$ spectrum was $A_{1,2}$. Therefore, the percentage contribution of the $K\alpha_{3,4}$ spectrum to the $K\alpha$ spectrum is $100 \times A_{3,4}/(A_{1,2} + A_{3,4})$ and the contribution of a particular satellite is $100 \times A_m/(A_{1,2} + A_{3,4})$.

A. Testing different calculation methods

The Cu $K\alpha_{3,4}$ spectral feature is well established as the $n = 2$ shake-off satellite [26,32,59,60]. However, there remains a question of whether it is generated by a $2p$ shake-off or a

TABLE VII. Comparison of clusters and spectral features with labels in the past literature and empirical fits: {[26] Fig. 3}; {[24] Fig. 19, Table 4} The labeling of approximate terms is neither unique nor transparent. Note the doublet and quartet wave functions are mixed in relativistic jj coupling.

Cluster		Approximate term values			Term used by [26,32]			*empirical labels*	
$\sim E$	*label*	Initial	→	Final	Initial	→	Final	[26]	[24]
$2p$ satellite			Tables III,V						
8059 eV	α_{34a}	$^2P_{1/2}, ^2P_{3/2}, ^4P_{5/2}$	→	$^2D_{3/2}, ^2P_{1/2}, ^4P_{3/2}$	$[^3P_1$	→	$^3P_1]$	–	–
8070 eV	α_{34b}	$^2P_{1/2}, ^2P_{3/2}$	→	$^4P_{3/2}$	$^3P_1$	→	$^3P_1$	α'	?α_{33}
8074 eV	α_{34c}	$^2P_{1/2}, ^2P_{3/2}$	→	$^2S_{1/2}$	$^3P_1$	→	$^3P_0$	–	–
8078 eV	α_{34d}	$^2P_{3/2}$	→	$^2P_{3/2}$	$^3P_2$	→	$^3P_2$	α_3	?α_{31}
8082 eV	α_{34e}	$^4P_{1/2}, ^4P_{3/2}, ^4P_{5/2}$	→	$^2P_{3/2}, ^2D_{5/2}$	$^1P_1$	→	$^1D_2$	α_4	?α_{32}
8085 eV	α_{34f}	$^2P_{1/2}$	→	$^2P_{1/2}, ^4P_{3/2}$	$^3P_0$	→	$^3P_1$	–	–
8087 eV	α_{34g}	$^2P_{1/2}, ^2P_{3/2}$	→	$^2P_{3/2}, ^2D_{5/2}$	$^3P_1$	→	$^3P_2$	α_3'	?α_{34}
8094 eV	α_{34h}	$^4P_{1/2}, ^4P_{3/2}$	→	$^2P_{1/2}, ^4P_{3/2}$	$^1P_1$	→	$^3P_1$	–	–
$2s$ satellite			Tables IV,VI						
8060 eV	α_{34i}	$^2S_{1/2}, ^4S_{3/2}$	→	$^2P_{1/2}$	$[^3S_1, ^1S_0$	→	$^3P_1, ^1P_1]$	–	–
8069 eV	α_{34j}	$^2S_{1/2}, ^4S_{3/2}$	→	$^2P_{1/2}, ^2P_{3/2}$	$[^3S_1, ^1S_0$	→	$^3P_1, ^1P_1]$	–	–
8080 eV	α_{34k}	$^2S_{1/2}, ^4S_{3/2}$	→	$^2P_{3/2}, ^4P_{5/2}$	$[^3S_1$	→	$^3P_{1/2}]$	–	–

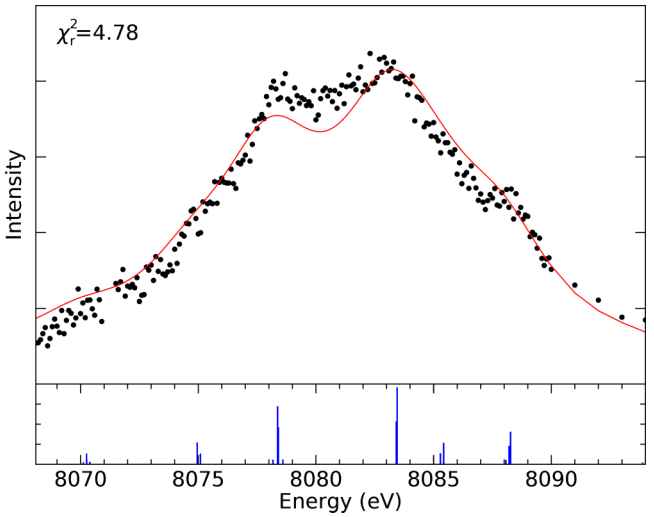

FIG. 5. The fit of our single configuration (4*s*) theory applied to the *M* spectrum. Each spectral feature aligns with our calculated energy eigenvalues, but a mismatch between the dominant transition intensity ratio causes residuals around the peak.

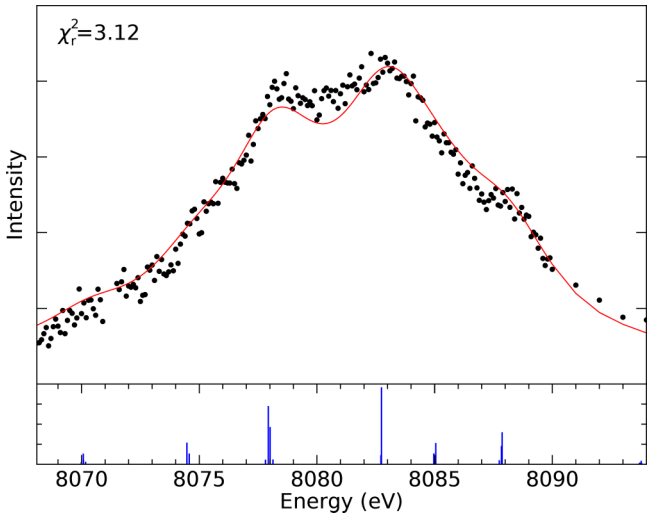

FIG. 6. Our fully converged (active set up to 5*p*) calculations of the $2p^5$ satellite applied to the Cu K$\alpha_{3,4}$ *M* spectrum. The full convergence is a clear improvement compared with Fig. 5.

combination of 2*p* and 2*s* shake-off with some intensity ratio, represented in our fit [Eq. (3)] by the ratio of A_{2s}:A_{2p}. Fritsch *et al.* [32] and Deutsch *et al.* [26] measured the Cu $K\alpha_{3,4}$ spectra and computed the 2*p* and 2*s* satellite structures using GRASP (1989) [61]. They obtained fits reporting a 2*s* satellite intensity of zero, which disagrees with *ab initio* shake probabilities. No biorthogonalization of the wave functions was included in that version of GRASP. Energies were calculated by subtracting the corresponding energy levels of the initial- and final-state wave functions and configuration interaction, of both the initial and final states, used to determine transition amplitudes. Therefore, these calculations were limited, reflected by the need to have a 1-eV energy offset of theory. Those approximations are not used in this work.

Herein, we consider two hypotheses. Hypothesis A, "that only the 2*p* satellite contributes" and Hypothesis B, "that both the 2*s* and 2*p* satellites contribute with some intensity ratio."

Using Hypothesis A, our single configuration (4*s*) results for the 2*p* satellite (top panel of Fig. 3) was applied to the M spectrum. Figure 5 shows that our 2*p* satellite MCDHF calculations recreate the profile of the Cu $K\alpha_{3,4}$ spectrum well. However, at this level of expansion, we can see that the ratio of the two dominant transitions is different from the experimental spectrum. Separately, an energy shift of 0.34 eV is required.

Fitting with our results expanded to the 5*s* level (lower panel of Fig. 3), we see a reduction in χ_r^2 from 4.78 to 3.05. As more CSFs are added, the atomic-state wave function approximation improves, reflected in a better match between theory and experiment (Fig. 6). These results support the claim that it is necessary both to expand the sets to higher shells for good convergence and to force certain orbitals to be inactive. The energy shift for this fit is 0.252 ± 0.022 eV, indicating that our MCDHF energy eigenvalues converged to within 0.252 eV of the experiment. This value can be used to represent the accuracy of our MCDHF energy eigenvalues: $0.25/8083 \approx 0.00003$ or 0.003% and hence supports the MCDHF method in obtaining highly accurate energy eigenvalues in the x-ray region.

The most recent theoretical investigation of the 2*p* satellite was performed by Nguyen *et al.* [36] as part of an extensive set of calculations on Cu $K\alpha$ and $K\beta$ diagram and satellite lines. Although that work made great strides on the various transition lines of Cu $K\alpha$ and $K\beta$ with convergence of up to 0.03 eV in accuracy, the authors noted that the calculation method they employed was not suitable for the 2*p* satellite, thus they did not believe that their results on this particular satellite had reached a satisfactory level of convergence or accuracy. In particular, Nguyen *et al.* [36] noted that their calculations for the $K\alpha$ 2*p* satellite had an energy fluctuation (or error estimation) of around 0.68 eV at the 5*s* expansion, which was far above their other satellite calculations, which

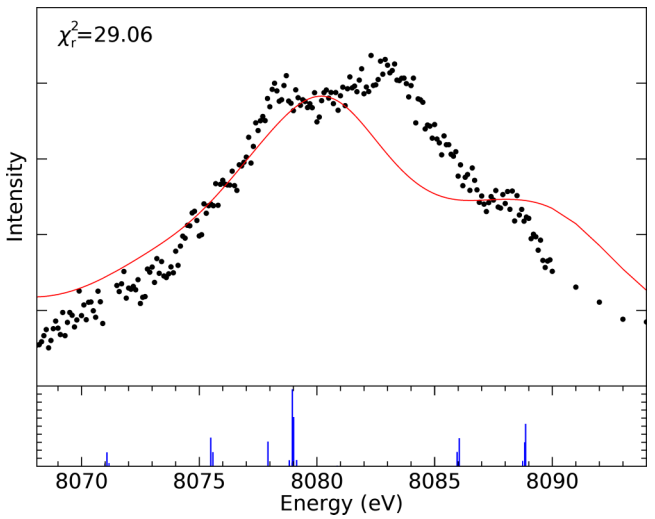

FIG. 7. Fit of the 5*s* stick diagrams of Nguyen *et al.* [36] to the M spectrum. The transition around 8082 eV is lost with the inclusion of the 4*s* orbital in the active set. By removing the 4*s* orbital from the active set, the full set of transitions is retained (Fig. 6).

TABLE VIII. Results of fitting using hypothesis *A* to each data set. The 4*s* row shows the results of fitting the single-configuration calculations and the 5*s* rows show the parameters of the fit when using our multiconfiguration results with an active set expanded to 5*s* and excluding 4*s*. The shift parameter of our multiconfiguration results suggest our energy eigenvalues converged to within 0.3 eV of experiment. The superior fits to the *M* spectrum suggest our theory more closely matches that data set.

Expanded to:	χ_r^2	Shift (eV) Fit to Mendenhall *et al.*	Width (eV)	% of Kα
4*s*	4.78	−0.34(2)	5.37(7)	0.856(3)
5*s*	3.05	0.25(2)	5.10(7)	0.791(3)
5*p*	3.12	0.25(2)	5.11(7)	0.791(3)
		Fit to Deutsch *et al.* (Gaussian broadening: HWHM = 0.8 eV)		
4*s*	14.05	−0.27(3)	3.07(6)	–
5*s*	9.872	0.26(3)	3.00(6)	–
5*p*	10.03	0.26(3)	3.00(6)	–

typically had an estimated error <0.05 eV. Moreover, when the 2*p* satellite calculation was expanded beyond the single configuration level, some transition lines were lost. This is a common problem with complex open-shell calculations and it is well known that in such situations the results are likely to be inaccurate. Figure 7 shows the 5*s* stick diagrams of [36] fitted to the M spectrum. The resulting $\chi_r^2 = 29.06$ validates the conclusion of Nguyen *et al.* [36] on their 2*p* satellite calculations. In this work, we resolved this convergence problem. The parameters resulting from each of these fits are shown in the top half of Table VIII.

B. Testing different data sets

As well as using experimental data to determine the validity of theoretical calculations it is possible to use theoretical calculations to support the use of one empirical data set over another. This is the case here. Performing the same fits as in Figs. 5–7 to the Deutsch *et al.* data yields the fits shown in the bottom half of Table VIII. Consistent with the original authors [32], these fits include a Gaussian broadening parameter with HWHM = 0.8 eV. Like the M spectrum, the best fit to the D spectrum is found using our results expanded to the 5*s* level (Fig. 8). Clearly, the theoretical values support the quality of the M data over that of the D data.

C. *I*(2*s*):*I*(2*p*) intensity ratio

Figure 6 assumes that the only satellite contributing to the $K\alpha_{3,4}$ spectral feature is the 2*p* satellite (hypothesis A). Previous work looked into the intensity ratio of contribution between the two satellites. However, the best fit was obtained with zero contribution from the 2*s* satellite, in contradiction with theory. The *ab initio* shake probabilities calculated by Mukoyama and Taniguchi [49] imply a $I(2s)$:$I(2p)$ ratio of 0.097:0.465, i.e., we should see a contribution from the 2*s* satellite of 17%.

To test whether the 2*s* satellite transition contributes to the $K\alpha_{3,4}$ spectrum we perform a fit using hypothesis B, where both satellite lines model the spectrum, and Eq. (3) with $A_{2p} + A_{2s} = 1$ so that the percentage contribution of each satellite to the $K\alpha_{3,4}$ spectrum may be determined as simply $A_m \times 100$. For this fit, two additional parameters are required, one for the extra width of the $2s^1$ satellite and one for its relative amplitude. The shift in energy was common to both satellites. The results (Fig. 9 and Table IX) indicate a contribution of the $2s^1$ multiplet to the $K\alpha_{3,4}$ spectral feature of 3.18(81)%. Importantly, including the $2s^1$ satellite in the model reduces the χ_r^2 from 3.12 to 2.79. A formal *F* test suggests that this improvement is significant and implies that hypothesis B describes the data better than hypothesis A. This is in contrast to what was found previously [26,32]. Figure 9 shows that the $2s^1$ contribution is heavily constrained by the transition at 8069 eV. Any fit with a large $2s^1$ contribution, as, for example, by Mukoyama and Taniguchi [49], would lead to an overestimation of the spectrum in this region.

These results raise questions about how to calculate satellite intensities. Our fitted intensities imply that the 2*s* satellite spectrum *does* contribute significantly to the $K\alpha_{3,4}$ spectrum. However, our contribution of 3.19(81)% is much smaller than that predicted by previous theory calculations [49]. To investigate this discrepancy, we will now calculate new copper *K*-edge shake probabilities.

VI. Cu *K*-SHELL SHAKE PROBABILITIES

In order for a spectator vacancy satellite to be observed, the ionizing particles must have sufficient energy to create an

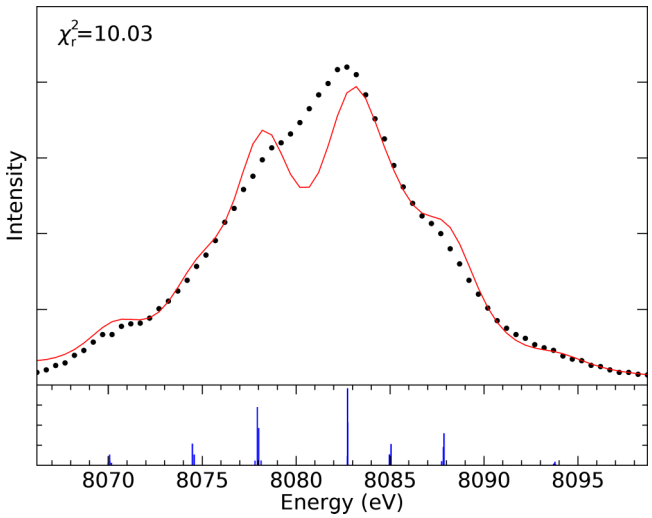

FIG. 8. This fit uses the same theoretical expansion as Fig. 6, applied to the D spectrum. Our theoretical predictions of the $K\alpha_{3,4}$ spectrum match the M spectrum more closely than the D spectrum.

TABLE IX. Fitted parameters of the Cu $K\alpha_{3,4}$ spectral feature using the atomic structure calculations for both the $2s$ and $2p$ satellites.

Hypothesis	χ_r^2	Shift (eV)	Satellite	Width (eV)	% of $K\alpha_{3,4}$	% of $K\alpha$
A	3.12	0.252(22)	$2p$	5.11(7)	100.00	0.79(1)
B	2.79	0.333(27)	$2p$	4.94(7)	96.81(72)	0.76(1)
			$2s$	2.39(72)	3.19(81)	0.03(1)

additional hole. In current theory, these additional holes are created through shake processes. Upon the sudden change in Hamiltonian, $\mathscr{H}(N+1) \rightarrow \mathscr{H}(N)$, the atom then relaxes to a state with an electron configuration other than the dominant $1s^{-1}$. For ionization energies well-above threshold, the probability of removing one or more electrons from the $n\kappa$ subshell, where n is the principal quantum number and κ is the relativistic quantum number [$\kappa = \mp(j+\frac{1}{2})$ for $j = l \pm \frac{1}{2}$], as a result of the sudden removal of a $1s$ electron, is given by

$$P_{n\kappa}^{\text{shake}} = 1 - (|\langle \Psi_{n\kappa}(N) | \tilde{\Psi}_{n\kappa}(N+1) \rangle|^2)^{M_{n\kappa}} - P_f, \qquad (4)$$

where $\Psi_{n\kappa}(N)$ represents the ionized atom with a $1s$ vacancy and $\tilde{\Psi}_{n\kappa}(N+1)$ represents the neutral atom [36]. The P_f term is a correction to avoid including the probability of shake-up to partially, or fully, occupied levels [62]. Equation (4) is equivalent to Eq. (5) of Nguyen *et al.* [36], but for a particular $n\kappa$ subshell.

The wave functions, $\Psi_{n\kappa}(N)$ and $\tilde{\Psi}_{n\kappa}(N+1)$ were calculated using the same method as we used to determine wave functions for the $2s$ satellite, i.e., the single configuration approximation was expanded to include all orbitals up to and including the $4f$ and then further expanded to include all orbitals to $5s$. In common with the $K\alpha$ satellite transition calculations, the $1s-2p$ orbitals were excluded from the active set during this process.

Equation (4) was used to calculate $P_{n\kappa}$ (the probability of shake occurring in a given orbital). The values were then transformed into *isolated shake-off probabilities* (the probability of a single electron being removed from a specific orbital, while all electrons in that orbital and in each of the other orbitals remain unchanged [36]). The results are shown in Table X.

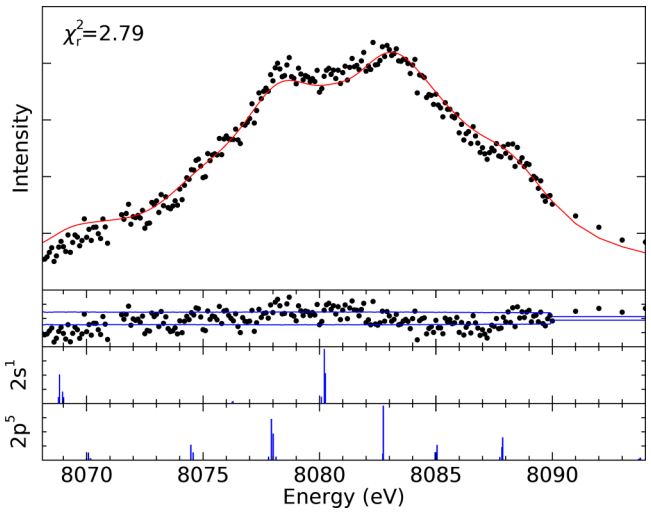

FIG. 9. Fit of the M spectrum allowing contributions from both the $2p$ and $2s$ satellite spectra. The improvement, in terms of χ_r^2, reveals that the $2s$ satellite is present. The full characterization is shown in Table IX. Below the fit, the residuals and one sigma uncertainly envelope are shown. The data required to recreate each of the stick diagrams are provided in Supplemental Material [57].

The current best standard for theoretical x-ray physics is to equate shake-off probabilities and satellite intensities [56,60,63]. Under this assumption, we can test the accuracy of our *ab initio* shake probabilities by comparing them with fitted satellite intensities, $K\alpha_{3,4}$ intensity and $2p$ shake probabilities (Table XI).

The value of Nguyen *et al.* [36] was obtained using a method that allows the development of shake probabilities with the expansion of the active set, however, this method requires more approximations. For the outer orbitals the shake probabilities reported by Nguyen *et al.* [36] are within 0.2% of the results presented here, indicating the approximations made in [36] affect the inner orbitals far more than the outer. Indeed, the approximation worked well for large overlaps' percentages and relatively poorly for small satellite probabilities.

Fitting using hypothesis A (Fig. 6) yields a $K\alpha_{3,4}$ contribution of 0.791(3)% and fitting via hypothesis B (Fig. 6) obtains 0.766(6)%, both slightly higher than the experimental values found by Mendenhall *et al.* [24] and Melia *et al.* [23]. The discrepancy between measures may be due to the background subtraction and different methods used.

The fits to experiment obtained using both hypothesis A and hypothesis B yield satellite intensities agreeing with our *ab initio* value to within 0.05%. This is a great success of the current work and approach. It also shows the similarity, during the fit, of hypothesis A and hypothesis B, which suggests the observed intensity of the $2s$ satellite is not dominant.

TABLE X. Shake probabilities as a result of the sudden removal of a Cu $1s$ electron. $P_{n\kappa}$ is calculated directly from Eq. (4). From our $P_{n\kappa}$ values, the isolated single shake probabilities, $P(n\kappa)$ and $P(nl)$, are calculated using the method outlined in Nguyen *et al.* [36]. The dominant double shake probabilities are $P(3d4s) = 1.147\%$ and $P(3d3d) = 0.825\%$.

	$P_{n\kappa}$%	$P(n\kappa)$%	$P(nl)$%
$1s$	0.192	0.143	0.143
$2s$	0.261	0.194	0.194
$2p+$	0.335	0.249	0.742
$2p-$	0.661	0.493	
$3s$	0.543	0.405	0.405
$3p-$	0.952	0.712	2.118
$3p+$	1.873	1.407	
$3d-$	5.923	4.567	11.664
$3d+$	9.052	7.097	
$4s$	8.954	7.298	7.298

TABLE XI. Comparison of Cu $K\alpha_{3,4}$ satellite intensities (integrated intensity % contribution to the total $K\alpha$ spectrum) and *ab initio* calculations of the $2p$ shake probability. Fitted intensities are determined by fitting Lorentzians to experimental data and examining the percentage contribution of the $K\alpha_{3,4}$ spectral feature to the total $K\alpha$ spectrum. Shake probabilities are determined using *ab initio* wave functions and the sudden approximation. Neglecting [36], the mean is 0.61 and standard deviation 0.18.

Fitted Intensity of $K\alpha_{3,4}$ satellite	%
Parratt [59]	0.6
Maskil and Deutsch [29]	0.74(15)
Illig *et al.* [64]	0.215(1)
Mendenhall *et al.* [24]	0.608
Melia *et al.* [23]	0.549(19)
This work hypothesis A	0.791(3)
This work hypothesis B	0.765(6)
2*p* Shake Probability	%
Mukoyama and Taniguchi [49]	0.465
Nguyen *et al.* [36]	3.39
This work	0.742

Our theoretical $2s$ shake probability of 0.194% is a factor of 10 larger than our fitted intensity of 0.03%. Performing the same fit with the ratio of the two intensities fixed according to our shake probabilities (Fig. 10) yields a χ_r^2 of 4.25 and a $2s$ width of 9.50(39) eV. This gives a $I(2s)$:$I(2p)$ ratio consistent with our theory, however, with significant residuals around the dominant peak. Hence, this is a serious discrepancy of the data from this theoretical model using the theoretical shake probabilities. Previous work speculated that the $2s$ satellite may be suppressed due to nonradiative processes [32]. We now consider the possibility and probability of such processes in the following section.

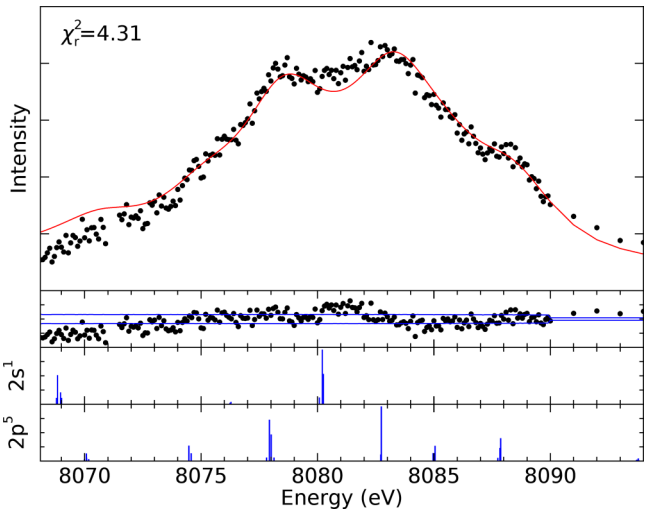

FIG. 10. Fit of the M spectrum with the satellite intensities fixed according to our shake probabilities. The agreement between the model and experimental data is significantly worse than when allowing the intensities to be free parameters. This strongly suggests an important physical process is not being modeled; addressed in the next section by considering the depopulation of the $2s$ satellite initial state through nonradiative processes.

VII. MCDHF NONRADIATIVE RATES

It is often assumed that a shake-off in some subshell leads to a satellite transition with a vacancy in that particular subshell. This assumption leads to the transition intensity A_m corresponding directly with the shake probability. A satellite transition for a $K\alpha$ spectrum is observed when the perturbation creating the initial $1s$ hole also creates another hole via a shake-off process, and the $2p \rightarrow 1s$ ($K\alpha$) electron transition takes place under an altered potential. Assuming the shake-off probability corresponds directly with the satellite intensity is valid only if the atomic relaxation always occurs first (fast) through the radiative $2p \rightarrow 1s$ electron transition and not via another means.

Let us now consider the Auger effect (a nonradiative transition) where an Auger electron is emitted rather than a photon. If a $2s$ shake-off vacancy is filled via an Auger transition before the $2p \rightarrow 1s$ transition, then we will no longer observe a $2s$ $K\alpha$ satellite photon. For example, a $L_1M_{2,3}M_{4,5}$ Auger transition could fill the $2s$ vacancy by creating two vacancies in the $3p$ and $3d$ orbitals. Then, the $2p \rightarrow 1s$ transition occurs in the presence of a $3p3d$ vacancy and we observe a $3p3d$ satellite rather than a $2s$. Copper, in particular, is open to many nonradiative decay processes due to its ten $3d$ electrons. To test the validity of this process being the leading factor behind the $2s$ satellite suppression, we performed calculations of rates for all possible nonradiative Auger transitions from an initial $1s2s$ or $1s2p$ hole. Rates resulting from an initial $1s3s$, $1s3p$, and $1s3d$ holes are included for completeness. These results are shown in Table XII.

The calculations were conducted using the multiconfiguration Dirac-Hartree-Fock method and implemented in the relativistic atomic transition, ionization, and recombination properties code, or RATIP [65,66]. The methodology follows recent work [67].

Implementing the RATIP suite of programs assumes that atomic-state functions (ASFs) were generated using GRASP2K. The methods for obtaining the ASFs are discussed in the previous section on MCDHF calculations, and the relevant citations, and therefore, we focus on the RATIP implementation once an initial ASF is obtained. For a bound initial state ψ_i and continuum final state $\psi_{f,\epsilon}$, the radiationless transition rate is

$$T_{i\rightarrow f} = 2\pi \left| \langle \psi_{f,\epsilon} | H - E | \psi_i \rangle + P \sum_{\beta=1}^{N} \int_0^\infty \frac{V_{f,\beta}(\epsilon,\tau,E)\,\langle \psi_{\beta\tau} | H - E | \psi_i \rangle}{E - E_\beta - \tau} d\tau \right|^2, \quad (5)$$

where ϵ, τ are the kinetic energies of the outgoing and intermediate state electrons, respectively, β runs across all continuum states, $V_{f,\beta}$, is the interaction matrix between different continuum states, and E is the initial hole-state energy [68–71].

For each of the relevant initial states, Table XII shows the rates of the two competing processes: the radiative $K\alpha$

TABLE XII. Transition rates of the competing processing possible after the creation of several initial states.

Initial hole	Final hole(s)	Type	Name	Rate ($eV/\hbar$)
$[1s]$	$[2p]$	Radiative	$K\alpha$ diagram	0.256
$[1s2s]$	$[2p2s]$	Radiative	$K\alpha$ $2s$ sat.	0.102
	$[1s2p3s]$	Auger	$L_1L_{2,3}M_1$	1.342
	$[1s2p3s]$	Auger	$L_1L_{2,3}M_{2,3}$	2.210
	$[1s2p3d]$	Auger	$L_1L_{2,3}M_{4,5}$	3.021
	$[1s2p4s]$	Auger	$L_1L_{2,3}N_1$	0.741
	$[1s3s3s]$	Auger	$L_1M_1M_1$	0.012
	$[1s3s3p]$	Auger	$L_1M_1M_{2,3}$	0.142
	$[1s3s3d]$	Auger	$L_1M_1M_{4,5}$	0.547
	$[1s3p3p]$	Auger	$L_1M_{2,3}M_{2,3}$	1.561
	$[1s3p3d]$	Auger	$L_1M_{2,3}M_{4,5}$	2.833
	$[1s3d3d]$	Auger	$L_1M_{4,5}M_{4,5}$	1.695
	$[1s3l4s]$	Auger	Σ LMN_1	<0.01
	Total $L_1(2s)$ Auger rate: 14.104			
$[1s2p]$	$[2p2p]$	Radiative	$K\alpha$ $2p$ sat.	0.257
	$[1s3s3s]$	Auger	$L_{2,3}M_1M_1$	0.019
	$[1s3s3p]$	Auger	$L_{2,3}M_1M_{2,3}$	0.119
	$[1s3s3d]$	Auger	$L_{2,3}M_1M_{4,5}$	0.508
	$[1s3p3p]$	Auger	$L_{2,3}M_{2,3}M_{2,3}$	1.342
	$[1s3p3d]$	Auger	$L_{2,3}M_{2,3}M_{4,5}$	1.240
	$[1s3d3d]$	Auger	$L_{2,3}M_{4,5}M_{4,5}$	1.891
	$[1s3l4s]$	Auger	Σ LMN_1	<0.01
	$2p$ total Auger rate: 5.299			
$[1s3s]$	$[2p3s]$	Radiative	$K\alpha$ $3s$ sat.	0.187
	$[1s3p3p]$	Auger	$M_1M_{2,3}M_{2,3}$	0.013
	$[1s3p3d]$	Auger	$M_1M_{2,3}M_{4,5}$	0.024
	$[1s3d3d]$	Auger	$M_1M_{4,5}M_{4,5}$	0.041
	$[1s3d4s]$	Auger	$M_1M_{2,3}N_1$	0.063
	$[1s3d4s]$	Auger	$M_1M_{4,5}N_1$	0.064
	$3s$ total Auger rate: 0.452			
$[1s3p]$	$[2p3p]$	Radiative	$K\alpha$ $3p$ sat.	0.140
	$[1s3p3p]$	Auger	$M_{2,3}M_{2,3}M_{2,3}$	0.00
	$[1s3d3d]$	Auger	$M_{2,3}M_{4,5}M_{4,5}$	<0.01
	$[1s3d4s]$	Auger	$M_{4,5}M_{4,5}M_{4,5}$	0.00
	$3p$ total Auger rate: <0.01			
$[1s3d]$	$[2p3d]$	Radiative	$K\alpha$ $3d$ sat.	0.103
	$[1s3d3d]$	Auger	$M_{4,5}M_{4,5}M_{4,5}$	0.00
	$[1s3d4s]$	Auger	$M_{4,5}M_{4,5}N_1$	<0.01
	$3d$ total Auger rate: <0.01			

satellite transition and the nonradiative transitions that depopulate the excited states. The depopulation of the $[1s2s]$ state via the Auger process has a total rate of 14.104 eV/$\hbar$ and is significantly larger than the $[1s2p]$ rate of 5.299 eV/$\hbar$. From this, we expect a suppression of the $2s$ satellite relative to the $2p$ satellite by a factor of (5.299/14.104). Furthermore, the relevant competing processes (the radiative rate of the satellite transitions) must also be considered and results in a further reduction by a factor of (0.257/0.102). Taking these into account, the expected $I(2s)$:$I(2p)$ intensity ratio changes from 0.194:0.742 (using only the shake probabilities) to 0.073 : 0.742, including the effect of nonradiative processes. Fitting with this new intensity ratio (Fig. 11) yields a χ^2_r of 2.79 and parameters shown in Table XIII. Hence this new model and ansatz is strongly supported by the experimental data.

TABLE XIII. Fitted parameters of the Cu $K\alpha_{3,4}$ spectral feature using the atomic structure calculations for both the $2s$ and $2p$ satellites and relative intensities tied to theory. Intensities are determined using *ab initio* theory, yet now the parameters of this characterization are consistent (within 2σ) with the parameters in Table IX, where the intensities were allowed to be free.

Hypothesis	χ^2_r	Shift (eV)	Satellite	Width (eV)	% of $K\alpha_{3,4}$	% of $K\alpha$
B	2.79	0.355(23)	$2p$	4.93(7)	95.54	0.76
			$2s$	3.13(34)	4.45(2)	0.04(1)

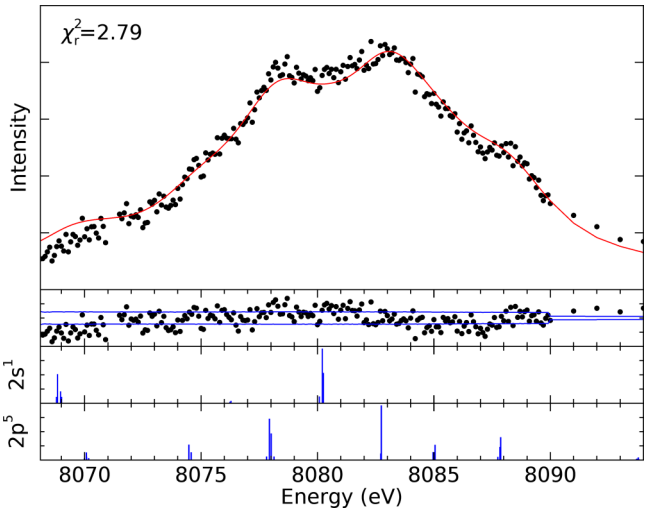

FIG. 11. Fit of the M spectrum using both the $2p$ and $2s$ satellite structures with a fixed intensity ratio. To fix the $I(2s)$:$I(2p)$ ratio, the shake probabilities and rates of competing processes are now included. The agreement between this fit and the fit shown in Fig. 9 (where the intensities were left as free parameters) demonstrates the accuracy of our nonradiative rates and that the depopulation of the $[1s2s]$ initial state is responsible for the suppression of the $2s$ satellite observed in experimental spectra.

These results demonstrate that the speculation regarding the suppression of the $2s$ satellite in the Cu $K\alpha_{3,4}$ spectrum is correct. The conclusion that the $2s$ satellite does not contribute at all is false. Instead, its relatively low intensity is explained by nonradiative pathways filling the $2s$ hole faster than the $K\alpha$ transition. This is the first time that the depopulation of the initial state through nonradiative processes was included in an *ab initio* calculation of x-ray radiation. The inclusion of the nonradiative Auger effect has resolved the discrepancy between the observed and calculated $2s$ satellite intensities in the copper $K\alpha_{3,4}$ spectrum.

The fit in Fig. 9 and Table IX is obtained with satellite intensities as free parameters, i.e, it is a semi-empirical result. Conversely, the fit in Fig. 11 and Table XIII has satellite intensities fixed according to *ab initio* theory. Introducing these constraints yields an almost identical χ_r^2 and parameters consistent with the earlier fit. This demonstrates the validity and precision of our method to include nonradiative pathways.

Without considering the depopulation of the initial state (i.e., when we fitted with intensities fixed to our *ab initio* shake probabilities) we obtained a χ_r^2 of 4.31. Including the effects of depopulation is critical to obtaining theoretical satellite intensities consistent with experiment and the atomic processes underpinning Cu $K\alpha_{3,4}$.

VIII. CONCLUSION

The quality of the high-accuracy $K\alpha$ measurements Fritsch *et al.* [32] and Mendenhall *et al.* [24] offered an avenue to test MCDHF theory to levels previously unobtainable. Therefore, new theoretical calculations on the copper $K\alpha_{3,4}$ satellite spectrum were performed. By fitting our calculations to the high-resolution data, we demonstrated that MCDHF and high-accuracy atomic theory with QED corrections is capable of determining the energy eigenvalues of satellite transitions to within 0.25 eV. A new set of *ab initio* shake probabilities for Cu is presented and these are shown to agree with fitted satellite intensities to within 0.2%. This then is a benchmark for the transferability and portability of data between experiments and compared with advanced theory.

However, given that the two data sets investigated are the most accurate in the literature, the discrepancy between them and the theoretical prediction deserves closer attention in the future. At this stage both confirm the accuracy of the theory; and the M spectrum (Mendenhall *et al.* [24]) appears superior. Of course, this raises new questions about the portability of experimental data sets and also how to collect the data in a way to represent atomic or quantum theory. These methods can be applied to other systems where conflicting data sets have no obvious method of determining which should be considered more reliable.

When fitting the satellite spectra to the data, several hypotheses were investigated. Hypothesis B shows a small but significant contribution of the $2s$ satellite with a χ_r^2 of 2.79 when the intensity ratio between the $2s$ and $2p$ were free. This resulted in a semi-empirical $2s$ satellite intensity an order of magnitude lower than *ab initio* shake off calculations. This anomaly now has strong evidence for being explained through the Auger process. By considering the rates of electron transition via both radiative and nonradiative pathways a new theoretically derived $2s$ satellite intensity is predicted. Using this intensity ratio value as a fixed parameter, the fit obtains a near identical χ_r^2. Hence, our final result on this topic is that the $2s$ satellite contributes significantly and with a fraction 0.04(1)% of the total copper $K\alpha$ spectrum or a percentage 4.45(1)% of the copper $K\alpha_{3,4}$ spectrum. This is strong evidence that nonradiative pathways must be considered when investigating *ab initio* shake probabilities or experimental characteristic and satellite spectra.

The avenue for further research into this topic will involve high-accuracy *ab initio* MCDHF computations of satellite spectra, amplitudes, Auger calculations, and atomic cascades [72] together with high-accuracy experimental data. Important questions of robustness and the portability of spectral profiles remain and are highlighted herein. Clearly, with many open and continuing questions, the characterization of x-ray spectra from open-shell systems remains a challenging and illuminating area of modern physics.

ACKNOWLEDGMENTS

The authors would like to acknowledge the Australian Research Council Grant No. DP210100795 and the Albert Shimmins Fund.

[1] M. Hansson, G. Berg, and M. Isaksson, X-Ray Spectrom. **37**, 37 (2008).

[2] M. Šmíd, O. Renner, A. Colaitis, V. T. Tikhonchuk, T. Schlegel, and F. B. Rosmej, Nat. Commun. **10**, 4212 (2019).

[3] A. M. Gojska, K. Koziol, A. Wasilewski, E. A. Mista-Jakubowska, P. Mazerewicz, and J. Szymanowski, Materials **14**, 4462 (2021).

[4] K. A. Weaver, J. Gelbord, and T. Yaqoob, Astrophys. J. **550**, 261 (2001).

[5] C. T. Chantler, T. V. B. Nguyen, J. A. Lowe, and I. P. Grant, Astrophys. J. **769**, 84 (2013).

[6] R. Duro, T. Dauser, V. Grinberg, I. Miskovicová, J. Rodriguez, J. Tomsick, M. Hanke, K. Pottschmidt, M. A. Nowak, S. Kreykenbohm, M. C. Bel, A. Bodaghee, A. Lohfink, C. S. Reynolds, E. Kendziorra, M. G. F. Kirsch, R. Staubert, and J. Wilms, Astron. Astrophys. **589**, A14 (2016).

[7] S. M. Mazzola, R. Iaria, T. Di Salvo, A. Sanna, A. F. Gambino, A. Marino, E. Bozzo, C. Ferrigno, A. Riggio, A. Anitra, and L. Burderi, Astron. Astrophys. **654**, A102 (2021).

[8] C. Lelièvre, A. Rouwane, I. Poirier, M. Bertrand, R. K. Gallon, and A. Murat, Environ. Technol. **42**, 4466 (2021).

[9] M. Cerdà-Domènech, J. Frigola, A. Sanchez-Vidal, and M. Canals, Sci. Total Environ. **717**, 134778 (2020).

[10] A. Turner and K. R. Solman, Talanta **159**, 262 (2016).

[11] A. Turner, Mar. Pollut. Bull. **124**, 286 (2017).

[12] A. Silva, C. Oliveira, A. Gouvêa, J. dos Santos, M. Carvalho, and J. Veloso, Anal. Bioanal. Chem. **395**, 2073 (2009).

[13] S. Pessanha, T. I. Madeira, M. Manso, M. Guerra, A. Le Gac, and M. L. Carvalho, Appl. Phys. A **116**, 1053 (2014).

[14] M. Guerra, M. Manso, S. Longelin, S. Pessanha, and M. L. Carvalho, J. Instrum. **7**, C10004 (2012).

[15] A. Silva, S. Cirino, M. Carvalho, M. Manso, S. Pessanha, C. Azevedo, L. Carramate, J. Santos, M. Guerra, and J. Veloso, Spectrochimica Acta Part B: Atomic Spectroscopy **129**, 1 (2017).

[16] M. Manso, A. Le Gac, S. Longelin, S. Pessanha, J. C. Frade, M. Guerra, A. J. Candeias, and M. L. Carvalho, Spectrochim. Acta-A: Mol. Biomol. **105**, 288 (2013).

[17] J. W. Dean, H. A. Melia, C. T. Chantler, and L. F. Smale, J. Phys. B: At. Mol. Opt. Phys. **52**, 165002 (2019).

[18] J. W. Dean, C. T. Chantler, L. F. Smale, and H. A. Melia, J. Phys. B: At. Mol. Opt. Phys. **53**, 205004 (2020).

[19] R. Yılmaz, Acta Phys. Pol. A **133**, 1227 (2018).

[20] M. J. MacDonald, A. M. Saunders, R. W. Falcone, W. Theobald, O. L. Landen, and T. Doppner, Rev. Sci. Instrum. **89**, 10F109 (2018).

[21] V. Koteswararao, K. R. Narayana, S. A. Sattar, B. Seetharamireddy, M. V. R. Murti, and A. D. P. Rao, Nucl. Instrum. Methods Phys. Res., Sect. B **499**, 107 (2021).

[22] J. L. V. Webster, J. D. Mcllquham, and B. Ganly, Radiat. Phys. Chem. **197**, 110173 (2022).

[23] H. A. Melia, C. T. Chantler, L. F. Smale, and A. J. Illig, Acta Crystallogr A Found Adv **75**, 527 (2019).

[24] M. H. Mendenhall, A. Henins, L. T. Hudson, C. I. Szabo, D. Windover, and J. P. Cline, J. Phys. B: At. Mol. Opt. Phys. **50**, 115004 (2017).

[25] M. Deutsch, G. Holzer, J. Hartwig, J. Wolf, M. Fritsch, and E. Forster, Phys. Rev. A **51**, 283 (1995).

[26] M. Deutsch, O. Gang, K. Hämäläinen, and C. C. Kao, Phys. Rev. Lett. **76**, 2424 (1996).

[27] H. H. Madden, D. M. Zehner, and J. R. Noonan, Phys. Rev. B **17**, 3074 (1978).

[28] R. E. LaVilla, Phys. Rev. A **19**, 717 (1979).

[29] N. Maskil and M. Deutsch, Phys. Rev. A **38**, 3467 (1988).

[30] N. Maskil and M. Deutsch, Phys. Rev. A **37**, 2947 (1988).

[31] G. Hölzer, M. Fritsch, M. Deutsch, J. Härtwig, and E. Förster, Phys. Rev. A **56**, 4554 (1997).

[32] M. Fritsch, C. C. Kao, K. Hamalainen, O. Gang, E. Forster, and M. Deutsch, Phys. Rev. A **57**, 1686 (1998).

[33] R. Diamant, S. Huotari, K. Hämäläinen, C. C. Kao, and M. Deutsch, Phys. Rev. Lett. **84**, 3278 (2000).

[34] M. Deutsch, E. Forster, J. Hartwig, K. Hamalainen, C. C. Kao, S. Huotari, and R. Diamant, J. Res. Natl. Inst. Stand. Technol. **109**, 75 (2004).

[35] C. T. Chantler, A. C. L. Hayward, and I. P. Grant, Phys. Rev. Lett. **103**, 123002 (2009).

[36] T. V. B. Nguyen, H. A. Melia, F. I. Janssens, and C. T. Chantler, Phys. Rev. A **105**, 022811 (2022).

[37] T. V. B. Nguyen, H. A. Melia, F. I. Janssens, and C. T. Chantler, Phys. Lett. A **426**, 127900 (2022).

[38] J. W. M. Du Mond and A. Hoyt, Phys. Rev. **36**, 799 (1930).

[39] L. G. Parratt, Phys. Rev. **50**, 1 (1936).

[40] H. J. Edwards and J. I. Langford, J. Appl. Crystallogr. **4**, 43 (1971).

[41] J. W. Dean, P. Pushkarna, H. A. Melia, T. V. B. Nguyen, and C. T. Chantler, J. Phys. B: At. Mol. Opt. Phys. **55**, 075002 (2022).

[42] L. Martins, P. Amaro, S. Pessanha, M. Guerra, J. Machado, M. L. Carvalho, and J. P. Santos, X-Ray Spectrom. **49**, 192 (2020).

[43] Y. Ito, T. Tochio, M. Yamashita, S. Fukushima, A. M. Vlaicu, J. P. Marques, J. M. Sampaio, M. Guerra, J. P. Santos, K. Słabkowska, E. Weder, M. Polasik, J. Rzadkiewicz, P. Indelicato, Y. Menesguen, M. C. Lepy, and F. Parente, Phys. Rev. A **102**, 052820 (2020).

[44] S. Schippers, R. Beerwerth, S. Bari, T. Buhr, K. Holste, A. L. D. Kilcoyne, A. Perry-Sassmannshausen, R. A. Phaneuf, S. Reinwardt, D. W. Savin, K. Schubert, S. Fritzsche, M. Martins, and A. Müller, Astrophys. J. **908**, 52 (2021).

[45] F. Bloch, Phys. Rev. **48**, 187 (1935).

[46] F. Bloch and P. A. Ross, Phys. Rev. **47**, 884 (1935).

[47] T. Åberg and J. Utriainen, Phys. Rev. Lett. **22**, 1346 (1969).

[48] E. H. Kennard and E. Ramberg, Phys. Rev. **46**, 1040 (1934).

[49] T. Mukoyama and K. Taniguchi, Phys. Rev. A **36**, 693 (1987).

[50] J. Campbell and T. Papp, At. Data Nucl. Data Tables **77**, 1 (2001).

[51] P. Jönsson, G. Gaigalas, J. Bieroń, C. F. Fischer, and I. Grant, Comput. Phys. Commun. **184**, 2197 (2013).

[52] J. A. Lowe, C. T. Chantler, and I. P. Grant, Radiat. Phys. Chem. **85**, 118 (2013).

[53] T. V. B. Nguyen, J. A. Lowe, T. L. H. Pham, I. P. Grant, and C. T. Chantler, Radiat. Phys. Chem. **204**, 110644 (2023).

[54] I. P. Grant, *Relativistic Quantum Theory of Atoms and Molecules* (Springer, New York, 2007).

[55] T. V. B. Nguyen, C. T. Chantler, J. A. Lowe, and I. P. Grant, Mon. Not. R. Astron. Soc. **440**, 3439 (2014).

[56] T. L. Pham, T. V. B. Nguyen, J. A. Lowe, I. P. Grant, and C. T. Chantler, J. Phys. B: At. Mol. Opt. Phys. **49**, 035601 (2016).

[57] See Supplemental Material at http://link.aps.org/supplemental/10.1103/PhysRevA.107.012809 for the output of GRASP2K describing the Cu K$\alpha 2s$ and $2p$ satellite transitions.

[58] A. Papoulia, J. Ekman, G. Gaigalas, M. Godefroid, S. Gustafsson, H. Hartman, W. Li, L. Radziute, P. Rynkun, S. Schiffmann, K. Wang, and P. Jonsson, Atoms **7**, 106 (2019).

[59] L. G. Parratt, Phys. Rev. **49**, 502 (1936).
[60] R. Diamant, R. Sharon, W. A. Caliebe, C.-C. Kao, and M. Deutsch, J. Phys. B: At. Mol. Opt. Phys. **39**, 651 (2006).
[61] K. G. Dyall, I. P. Grant, C. T. Johnson, F. A. Parpia, and E. P. Plummer, Comput. Phys. Commun. **55**, 425 (1989).
[62] M. O. Krause and T. A. Carlson, Phys. Rev. **158**, 18 (1967).
[63] S. P. Limandri, R. D. Bonetto, A. C. Carreras, and J. C. Trincavelli, Phys. Rev. A **82**, 032505 (2010).
[64] A. J. Illig, C. T. Chantler, and A. T. Payne, J. Phys. B: At. Mol. Opt. Phys. **46**, 235001 (2013).
[65] S. Fritzsche, J. Electron. Spectrosc. Relat. Phenom. **114-116**, 1155 (2001).
[66] S. Fritzsche, Comput. Phys. Commun. **183**, 1525 (2012).
[67] J. W. Dean, C. T. Chantler, and B. Ganly, Radiat. Phys. Chem. **200**, 110472 (2022).
[68] G. Howat, T. Åberg, and O. Goscinski, J. Phys. B **11**, 1575 (1978).
[69] K. R. Karim and B. Crasemann, Phys. Rev. A **31**, 709 (1985).
[70] S. Fritzsche, B. Fricke, and W. D. Sepp, Phys. Rev. A **45**, 1465 (1992).
[71] S. Fritzsche and A. Surzhykov, Molecules **26**, 2660 (2021).
[72] S. Fritzsche, P. Palmeri, and S. Schippers, Symmetry **13**, 520 (2021).